Received <day> <Month>, <year>; | Revised <day> <Month>, <year>; | Accepted <day> <Month>, <year>

DOI: xxx/xxxx

ARTICLE TYPE

Fully Coupled Numerical Model of Actin Treadmilling in the Lamellipodium of the Cell

K.S. Kollepara[1] | P.D. Mulye[1] | P. Saez*[2]

[1]Ecole Centrale de Nantes, 1 Rue de la Noe, 44300 Nantes, France

[2]Laboratori de Calcul Numeric (LaCaN), Universitat Politécnica de Catalunya–BarcelonaTech (UPC), Jordi Girona 1-3, 08034 Barcelona, State name, Spain

Correspondence

*P. Saez. Email: pablo.saez@upc.edu

Abstract

Cells rely on an interplay of subcellular elements for motility and migration. Certain regions of motile cells, such as the lamellipodium, are made of a complex mixture of actin monomers and filaments which polymerize at the front of the cell, close to the cell membrane, and depolymerize at the rear. The dynamic actin turnover induces the so-called intracellular retrograde flow and it is a fundamental process for cell motility. Apart from some comprehensive mathematical models, the computational modelling of actin treadmilling has been based on simpler biophysical models. Here, we adopt a highly detailed theoretical model of the actin treadmilling process and develop a coupled unsteady finite element formulation. We clearly describe the structure and implementation of the coupled problem within the finite element method. Our numerical results show an excellent correlation with experimental results from literature and with previous models. We include time dependent effects and convective transport terms, which expose puzzling dynamics in the retrograde flow. We propose several biological scenarios to analyze the behavior of the actin treadmilling along space and time. We observed response times of the main density variables in the order of seconds. Compared to previous analytical solutions, which make assumptions related to convective transport, transient dynamics and actin fluxes, the generic solution can have significant influence on the retrograde flow. All together, our results unveil a promising applicability of classical finite element methods to derive an in-silico testing platform for the actin treadmilling processes in motile cells, which could allow for an extension to other biophysical effects.

KEYWORDS:

Cellular physics, Actin Treadmilling, Finite Element Method, Coupled-problems

1 | INTRODUCTION

Actin dynamics is unarguably a fundamental element in cell motility, migration and morphology [27, 37, 38]. An explicit understanding of the actin cycle at different spatial and temporal scales of the cell have been, and still is, a jigsaw in biology. Actin dynamics control a wide range of cellular processes and it has been proposed as a key player in the protrusion of the leading edge[39]. The continuous movement of actin in the cell body, a flow of cellular components from the outer margin of the cell to the rear of the cell induce the so called retrograde flow. The retrograde flow is dictated by either a passive or an active movement of actin that polymerizes against the plasma membrane and can be pulled and transported by other phenomena. More important, retrograde flow have been identified as the major contributor for cell motility [7, 33, 37].

Cell motility can be categorized as a function of its velocity. Classical models of slow motility are epithelial cells and fibroblast while keratocytes stands as a widely accepted model for fast cells. Actin turnover remains almost stationary along cell progression in fast moving cells and the actin treadmilling is mainly used for a continuous protrusion for the leading edge [47, 51]. On the contrary, slow cells transform the continuous flow of actin on the leading edge into a notably retrograde flow [49, 46, 25], unveiling a key distinctive feature between both cell models. Actually, the degree at which protrusion occurs in comparison with the retrograde flow has been suggested as a clear indicator of fast versus slow cells. Nonetheless, in contradiction with other reports, retrograde flow has been also distinguished in keratocytes [48, 17]. Such differences and similitudes raise the question whether a given cell possess the same control mechanism or if differences just arise in the spatial and temporal organization of all the actors involved. For example, the retrograde flow can present non-uniform fields over the cell domain. In the rear of keratocytes, where myosin concentrates, the retrograde flow is faster than on the periphery of the cell [51].

1.1 | Actin Dynamics

The regulation of the actin treadmilling is the most remarkable and widely studied process (see, e.g, [27, 37, 38] in the mechanism of retrograde flow. In short, the actin dynamic turnover is dictated by a continuous assembly and disassembly of different cellular constituents. Actin monomers nucleate, promoted by Formin, Profilin and cofilin [22, 10], and polymerize rapidly after a period of slow nucleation [38, 5]. Actin filaments, F-Actin, are identified as polar (all monomers pointed in the same direction) acquiring a fast-growing end, the (+) end or barbed end, and a slow dissociating end, the (-) end or the pointed end. The constant growth of the F-actin through the polymerization of the barbed ends pushes the filaments backwards to be balanced by the depolymerization mechanism along the lamellipodium of the cell at the pointed ends of the F-actin. During this process the association and disassociation rates control the rate of filament formation [5]. Furthermore, F-Actin undergoes a complex reaction while assembling and disassembling. Barbed ends terminate its formation when capping proteins associate in a process referred as capping [8], which inhibites further growth. The process of capping and uncapping in the leading edge is still not well understood but a number of proteins have been described to control both the uncapping and capping of barbed ends [6, 36]. F-Actin dissociates, mediated by ADP and cofilin, at the pointed-end producing ADP-actin dissociations. Then, profilin promotes the ATP replacement of ADP, providing a pool of new actin monomer ready to bind the barbed ends [37, 5]. A key actor in the actin turnover is the nucleation promoting factor Arp2/3. Arp2/3 activates and promotes the formation of new branches of actin filament along the barbed end of the actin filament [2]. The Arp2/3-dependent formation [31, 2] of actin filaments has been experimentally demonstrated [32, 38].

Apart from the actin dynamics briefly described above, myosin motor can also regulate the dynamics of the actin retrograde flow as it has been demonstrated in neural growth cones [24] and keratocytes [51]. In fact, this coupling establishes the active mechanism required for cell crawling [45, 51]. In few words, the motor domain of myosin, a superfamily of ATP-dependent motor proteins, binds to F-actin and generate force via ATP hydrolysis to move along the filament towards the barbed end [14]. [51] showed the role of the non-muscle myosin II in the disassembling actin network. [52] demonstrated that the actin-myosin organization could be in charge to initiate polarization of the cell and further cell motility. There is still an open debate about the role of different types of myosin in overall dynamic behavior of the actin-myosin complex cell mechanics and retrograde flow in particular.

1.2 | Mathematical and Computational Models

Mathematical and computational models have been extensively used [16, 13] to unravel open questions in cell motility. The foundations of actin treadmilling have been mathematically established [35, 29, 4, 41] and more and more detailed models have appeared [19, 23, 4]. Some models couple the actin treadmilling with the mechanics of the membrane protrusion [34, 28, 11]. The most detailed theoretical models today (see, among others, [29, 4] have been solved either analytically or in simple 1D numerical schemes. However, they have not been extended to more complex 2- and 3D geometries. Therefore, there is a need to incorporate the latest modeling developments in the actin treadmilling process into classical numerical schemes so that they could provide new insights.

In this work, we adopt one of the most complete theoretical models of actin treadmilling [29] and develop a fully coupled finite element model. We aim to describe through numerical methods how all the constituents involved in the retrograde flow work together. We focus on fast motile cells, such as keratocytes, where both the protrusion and the retrograde flow speed remains steady along cell crawling. Moreover, we focus on a portion of the front of the cell, as highlighted in Fig. 1 . We can choose our frame of analysis as a system of reference that moves at constant speed with the cell. We will call this the cell frame system while the movement of the cell will be defined from a reference cartesian system. The paper is organized as follow: First, we describe the basic equations describing the complex transport problem in cell mechanics. Second, we particularize the transport

problem for the pool of actin monomers as well as actin filaments. We focus then in the numerical implementation by using the finite element method, where the temporal and spatial discretization are discussed. Then we describe in detail the linearized coupling procedure needed for a Crank-Nicolson implicit formulation. Third, we present several results for physiological conditions as well as drug treated-like situations, usually described in experimental results. Finally, we discuss our methodology and results.

2 | GOVERNING EQUATIONS

2.1 | The Actin Treadmilling Model

We consider here the turnover of G-actin and F-actin in several of its forms. The model is adopted from [29] which is one of the most complex and the most accurate model developed up to date. We first consider the dynamics of barbed ends, defined as ρ^B. Barbed ends are the filament ends pointing towards the cell membrane and with fast-growing dynamics. Uncapped minus ends (ρ^m), those still available for polymerization of actin monomers with the fuelling ATP attached, are concentrated close to the leading edge and therefore they can be described per unit length of the membrane. The variable describing the process of capping of the minus ends is denoted by ρ^{mc}. The disassembling process has been described as follow. The ATP attached to actin hydrolyze and are converted to ADP. The hydrolyzed ADP-F-actin attach to ADF-cofilin, promoting its dissociation into fragments, denoted here by ρ^s, that at the same time creates new uncapped pointed ends (ρ^m). Profilin makes the ADP to ATP exchange possible, creating ATP-G-Actin-profilin complexes (ρ^a) which will be later used at the leading edge by the barbed end for the nucleation process. Finally, ATG-Thymosin, denoted by ρ^β, depletes or promotes the amount of ATP-G-Actin-profilin which increases the ATP form of G-actin. The depolymerization of the actin filaments plays a key role not only for keeping the extension of the filaments within the cell margins but for providing a pool of actin monomers in the lamellipodium to be recycled at the leading edge. We have summarized the main substances involved in the process in Fig. 1 (c). All constituents considered in the model are tabulated in Fig. 1 (b). In the following section we describe in detail the mathematical modeling adopted for each F-actin and G-actin form.

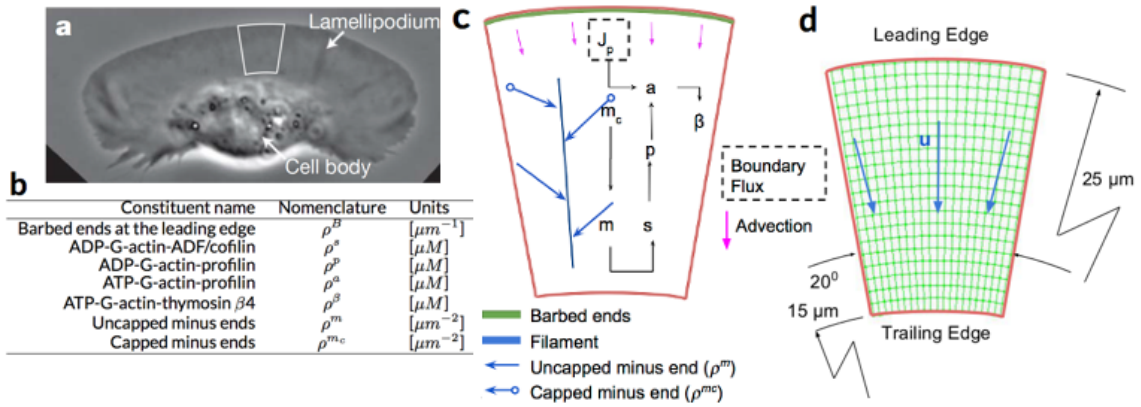

FIGURE 1 Top left: Keratocyte cell, adapted from [51]. The region of interest highlighted in white. Bottom left: the model is described through 7 different forms of actin. The model takes into account the density of the barbed ends ρ^B at the leading edge of the lamillopod as well as the dynamics of the pointed ends, described by the uncapped and capped forms ρ^m and ρ^{mc}. The pool of G-actin monomers is also described. The densities of ADP-G-actin sequestered by ADF/cofilin ρ^s, the exchange of ADP-G-actin to ATP-G-actin-profilin and ATP-G-actin-thymosin β_4 complexes are also considered and denoted by ρ^a and ρ^β respectively. Middle: we sketch the domain of interest, corresponding to the central section of the cell. The figure shows the main interaction between the main structures and components in the actin turnover process, which is modeled through Eq.5-12. Right: Details of the geometry analyzed.

2.2 | Problem Statement

Consider the following advection-diffusion-reaction model for the evolution of the concentration $\rho^i = \rho^i(\mathbf{x}, t)$ of a constituent i within the lamellipodium of the cell as

$$\partial_t \rho^i + \mathbf{u} \cdot \nabla \rho^i - \nabla \cdot (\nu \nabla \rho^i) + \sigma \rho^i = s(\rho^j) \quad \text{in } \Omega,\ t > 0 \tag{1}$$

$$\rho^i(\mathbf{x}, t) = \rho^i_d(\mathbf{x}, t) \quad \text{on } \Gamma_D,\ t > 0 \tag{2}$$

$$\partial_n \rho^i(\mathbf{x}, t) = h^i_n(\mathbf{x}, t) \quad \text{on } \Gamma_N,\ t > 0 \tag{3}$$

$$\rho^i(\mathbf{x}, 0) = \rho^i_0(\mathbf{x}) \quad \text{in } \Omega \tag{4}$$

where $\Omega \in \mathbb{R}^2$ is the domain of interest with boundary $\partial\Omega$ such that $\partial\Omega = \Gamma_D \cup \Gamma_N$ where Γ_D and Γ_N are the Dirichlet and Neumann boundaries respectively. The vector field $\mathbf{u}$ represents the advection velocity, ν is the diffusion coefficient and σ is the reaction coefficient. $s(\rho^j)$ is the source term for the creation and removal of material which depends on the concentration of other constituents of the system. The reaction term is treated as a reaction if it has a constant coefficient. Any non-linearities or couplings with other concentration variables are treated inside the source term, with the exception of the convection velocity u. Finally, ρ^i_d and h^i_n are given functions for the Dirichlet and Neumann boundary conditions respectively. The entire cell treadmilling can be described by means of combination of this general transport equation for each constituent. In Fig. 1 we summarize the interplay between the different constituents i, which accounts for the different elements of the actin turnover.

2.3 | Dynamic of Actin Monomers

First we describe the complex interplay between the different forms of actin monomers. We account for four forms of the actin monomers concentration (see Fig. 1). Following [29], we consider the concentration of ADP-G-actin-ADF/cofilin ρ^s, ADP-G-actin-profilin ρ^p, ATP-G-actin-profilin ρ^a and ATP-G-actin-tymosin ρ^β. These forms of actin account for the sequestering due to three main proteins, ADF/cofilin, profilin and thymosin. ρ^s and ρ^p represents the dynamics of ADP-G-actin sequestered by cofilin and profilin, while ρ^a and ρ^β represents the dynamics of ATP-G-actin sequestered by thymosin and profilin, respectively. This set of equations can be modeled as follow:

$$\partial_t \rho^s + \mathbf{u} \cdot \nabla \rho^s - \nabla \cdot (\nu^s \nabla \rho^s) + \sigma^s \rho^s = s^s(\rho^p, \rho^m), \tag{5}$$

$$\partial_t \rho^p + \mathbf{u} \cdot \nabla \rho^p - \nabla \cdot (\nu^p \nabla \rho^p) + \sigma^p \rho^p = s^p(\rho^s), \tag{6}$$

$$\partial_t \rho^\beta + \mathbf{u} \cdot \nabla \rho^\beta - \nabla \cdot (\nu^\beta \nabla \rho^\beta) + \sigma^\beta \rho^\beta = s^\beta(\rho^a, \rho^p) \text{ and} \tag{7}$$

$$\partial_t \rho^a + \mathbf{u} \cdot \nabla \rho^a - \nabla \cdot (\nu^a \nabla \rho^a) + \sigma^\beta \rho^a = s^a(\rho^\beta, \rho^p). \tag{8}$$

We define the following reaction and source terms:

$$\sigma^s = k_1 \in \mathbb{R}^+ \quad \text{and} \quad s^s(\rho^p, \rho^m) = k_{-1}\rho^p + j_d \tag{9}$$

$$\sigma^p = k_{-1} + k_2 \in \mathbb{R}^+ \quad \text{and} \quad s^p(\rho^s) = k_1 \rho^s \tag{10}$$

$$\sigma^a = k_3 \in \mathbb{R}^+ \quad \text{and} \quad s^a(\rho^\beta, \rho^p) = k_{-3}\rho^\beta + k_2 \rho^p \tag{11}$$

$$\sigma^\beta = k_{-3} \in \mathbb{R}^+ \quad \text{and} \quad s^\beta(\rho^a, \rho^p) = k_2 \rho^p - k_3 \rho^a \tag{12}$$

The above equations define the complex association and dissociation kinetics of actin filaments. Equations [5-8] satisfy no-flux boundary conditions at the front and rear of the cell. The source term $j_d = V_{dep}/(\delta\eta)\rho^m$ defines ADP-G-actin-ADF/cofilin being formed due to disassembling of F-actin. Here, V_{dep} represents the rate of depolymerization of the filaments. Just the ATP-actin-profilin, ρ^a, that is used in the leading edge during polymerization, fulfils

$$J_p = \left(-D\frac{\partial \rho^a}{\partial \mathbf{n}} + \mathbf{u}\rho^a\right)\Big|_{front} = -\frac{V}{\delta\eta}\rho^B\Big|_{front} \tag{13}$$

The flow of ρ^a in the boundary points toward the cell membrane. J_p is defined by the addition of monomer per filament $\delta[nm]$, the protrusion velocity V[$\mu m/s$] (discussed below) and the density of uncapped barbed end ρ^B in the leading edge. The factor η converts the flux [$\mu m^{-1}s^{-1}$] into [$\mu M s^{-1}$] (see [29] for more details).

2.4 | Dynamic of Actin Filaments

ρ^m and ρ^{m_c} represent the concentration of actin filaments still capped by Arp2/3 and pointed end filaments. In short, we can write the overall actin filament turnover following the mathematical description in [29]:

$$\partial_t \rho^{m_c} + \mathbf{u} \cdot \nabla \rho^{m_c} + \sigma^{m_c} \rho^{m_c} = s^{m_c} \quad \text{in } \Omega,\ t > 0 \tag{14}$$

$$\partial_t \rho^{m} + \mathbf{u} \cdot \nabla \rho^{m} + \sigma^{m} \rho^{m} = s^{m} \quad \text{in } \Omega,\ t > 0. \tag{15}$$

σ^{m_c} describes the rate of uncapping in the pointed ends. Capped ends are not generated in the interior of the cell, which motivates to set $s^{m_c} = 0$. We also assume that s^m acts as a negative source term in the dynamics of the pointed ends. The reaction term σ^m accounts for the half life of the actin filament. The total concentration of barbed ends in the domain is represented by ρ^B. The time derivative of ρ^B can be defined at the leading edge as $\partial_t \rho^B + \sigma^B \rho^B = s^B$. The terms σ^B represent the half life of capping barbed ends. s^B $[s^{-1}\mu m^{-1}]$ is the rate of branching barbed ends promoted by Arp2/3. In summary, we can describe the reaction and source terms as

$$\sigma^B = \gamma \in \mathbb{R}^+ \quad \text{and} \quad s^B = n \in \mathbb{R}^+, \tag{16}$$

$$\sigma^{m_c} = \tau_1 \in \mathbb{R}^+ \quad \text{and} \quad s^{m_c} = 0 \tag{17}$$

$$\sigma^{m} = \tau_2 \in \mathbb{R}^+ \quad \text{and} \quad s^{m}(\rho^{m_c}) = \tau_1 \rho^{m_c} \in \mathbb{R}^+ \tag{18}$$

To furnish (14) with appropriate boundary conditions the following physical observations are assumed. The terms proportional to ρ^{mc} and ρ^m describe the uncapping of minus ends and removing of uncapped minus ends due to the disassembly of the actin filaments, respectively. Capped pointed ends are capped at the same rate as barbed ends at the leading edge where the flux of capped ends must equal the nucleation rate n. The density of capped and minus ends at the leading edge are $\rho^{m_c}(LE, 0) = n/V$ and $\rho^m(LE, 0) = 0$. Here, LE denotes the leading edge. The rate of capping and branching are assumed constant since the amount of Arp2/3 is the limiting factor in the growing process and the amount of branching sites is in abundant supply. Therefore, the density of filaments capped with Arp2/3 are described by the constant nucleation rate divided by the velocity of the leading edge. At the front and rear edges the concentrations are assumed to fulfill no-flux boundary conditions. A schematic representation of the constituents and their interactions are shown in Fig. 1 .

These equation can be dramatically simplified if the transient and convective terms are neglected. See [29] for a complete discussion. One of the most important results of this simplification is obtained by substituting Eq. 14 in the definition of j_d in the previous section, obtaining a simplified form of the flux. Following this reasoning, we can obtain that $j_d \approx 7\mu M s^{-1}$. Following further assumptions, the form of the polymerization flux can be also simplified as $J_p = L j_d$. Both assumptions has been described in depth in [29] and simplifies the coupling between the velocity and the density profiles.

2.5 | Protrusion and Moving Velocity

A key aspect in the model is the definition of the different velocities involved in the model. We define in this section the protrusion and moving velocity of the cell, which is directly related with the velocity of the retrograde flow (see [29, 3] for further discussion). It is important to note that we define our problem in the cell frame, meaning that we follow the cells as it moves. We start by recalling some physical models of membrane protrusion. Let's consider a free polymerization velocity, meaning that the constant actin assembly do not face any restriction as it moves. In this situation we can define the free polymerization velocity as

$$V_0 = k_{on} \rho^a(LE, 0). \tag{19}$$

k_{on} defines the constant rate of actin nucleation and $\rho^a(LE, 0)$ is the density of ATP-G-actin-profilin at the front of the cell. We weight the product of these two variables by the length of one single actin monomer. However, actin filaments grow against a resistance membrane, the cell membrane. Following previous physical reasonings [34, 28, 29], the final protrusion velocity has been approximated as

$$V = V_0 exp(-F\delta/\rho^B k_b T), \tag{20}$$

where F represents the resistance force of the cell membrane per unit length [pN/μm]. The thermal energy constant is $k_b T = 4.1[pN \cdot nm]$.

Let's now consider the velocity of the actin network in the coordinate system of the moving cell, therefore moving with the cell at a velocity V. The moving velocity can be approximated by

$$V = -\mathbf{u}(\mathbf{x}, t) \cdot \mathbf{n}. \tag{21}$$

Any substance within the cell will drift at a rate $\mathbf{u}(\mathbf{x}, t)$.

3 | NUMERICAL APPROXIMATION

Next, we provide the basic ingredient for the complete temporal and spatial discretization of the parabolic equations presented in (5-8) and (14-16). The reader is referred to [15] for a detailed description and overview.

3.1 | Time Discretization

The time integration of our set of equations is performed through the θ family methods, which are based on a weighted average of ρ_t^n and ρ_t^{n+1} within a truncated Taylor expansion of order $\mathcal{O}((1/2-\alpha)\Delta t, \Delta t^2)$. The temporal discretization is given by a time interval $\mathcal{T}$ and a number of subintervals n, $\mathcal{T} = \bigcup_0^{n-1}[t^n, t^{n+1}]$, with a time increment $\Delta t = t^{n+1} - t^n \geq 0$. The temporally discretized form of the general parabolic equation (1) reads

$$\frac{\rho}{\Delta t} + \theta\mathcal{L}(\rho) = \frac{\rho^n}{\Delta t} - (1-\theta)\mathcal{L}(\rho^n) + \theta s + (1-\theta)s^n \tag{22}$$

Here, we define the operator $\mathcal{L}(\bullet) = \mathbf{u}\cdot\nabla - \nabla\cdot(\nu\nabla) + \sigma$ acting on ρ. Note that for sake of simplification of notation, the superindex i in the previously denoted ρ^i in (1) and the superindex for the time increment $n+1$ have been dropped from now on. We adopt the classical implicit 2^{nd} order by choosing $\theta = 1/2$.

3.2 | Weak Form of the Convection-Diffusion Equation

We focus next on the spatial discretization of the problem. Following the standard Galerkin formulation for the weak form of the initial boundary value problem we define a set of weighting functions and admissible solutions. The trial function $\mathcal{S}$ are required to fulfill the Dirichlet condition in Γ_D. The test function $\mathcal{V}$ are all functions that are square integrable, have square integrable first derivatives in Ω and vanish in Γ_D. Writing these spaces in a mathematical fashion, and recalling the usual Hilbert spaces, we can define

$$\begin{aligned}\mathcal{S}_t &= \{\rho|\rho(\cdot,t)\in\mathcal{H}^1(\Omega)\ t\in[0,T]|\ \rho(\mathbf{x},t) = \rho^d \text{ on } \Gamma_D\}\\ \mathcal{V} &= \{\omega\in\mathcal{H}^1(\Omega)\mid \omega = 0 \text{ on } \Gamma_D\}\end{aligned} \tag{23}$$

By using these solution spaces and weighted residuals the weak form reads

$$\int_\Omega \omega\frac{\rho}{\Delta t}\mathrm{d}\Omega + \theta\int_\Omega \omega\mathcal{L}(\rho)\mathrm{d}\Omega = \int_\Omega \omega\frac{\rho^n}{\Delta t}\mathrm{d}\Omega - (1-\theta)\int_\Omega \omega\mathcal{L}(\rho^n)\mathrm{d}\Omega + \int_\Omega \omega[\theta s + (1-\theta)s^n]\mathrm{d}\Omega \tag{24}$$

By applying the Gauss theorem on the second term of the left hand side of the previous equation, considering the boundary such that $\partial\Omega = \Gamma_D\cup\Gamma_N$ and using $\nu\partial_n\rho + \mathbf{u}\cdot\nabla\rho = h_N$ on Γ_N the problem can be written in a compact form as:
find $\rho\in\mathcal{S}_t$, for any $t\in[0,T]$ such that all weighing functions in $\omega\in\mathcal{V}$

$$\begin{aligned}(\omega,\frac{\rho}{\Delta t}) + \theta[a(\omega,\rho) + c(\mathbf{u};\omega,\rho) + (\omega,\sigma\rho)] =\\ (\omega,\frac{\rho^n}{\Delta t}) - (1-\theta)[a(\omega,\rho^n) + c(\mathbf{u};\omega,\rho^n) + (\omega,\sigma\rho^n)] + \theta(\omega,s) + (1-\theta)(\omega,s^n) + \theta(\omega,h)_{\Gamma_N} + (1-\theta)(\omega,h^n)_{\Gamma_N}\end{aligned} \tag{25}$$

where each of the operators can be defined as

$$(\omega,\rho) = \int_\Omega \omega\rho\mathrm{d}\Omega, \qquad c(\mathbf{u};\omega,\rho) = \int_\Omega \omega\mathbf{u}\cdot\nabla\rho\mathrm{d}\Omega, \qquad a(\omega,\rho) = \int_\Omega \nabla\omega\cdot(\nu\nabla\rho)\mathrm{d}\Omega \quad \text{and} \qquad (\omega,\rho)_{\Gamma_N} = \int_{\Gamma_N}\omega\rho\mathrm{d}\Gamma. \tag{26}$$

By analogy with the previously defined spatial operator, we define an associated form as

$$\hat{\mathcal{L}}^\omega(\bullet) = \int_\Omega \omega\mathbf{u}\cdot\nabla(\bullet)\mathrm{d}\Omega + \int_\Omega \nabla\omega\cdot(\nu\nabla(\bullet))\mathrm{d}\Omega + \int_\Omega \omega\sigma(\bullet)\mathrm{d}\Omega \tag{27}$$

so that we can rewrite the weak form in a more compact form as

$$(\omega,\frac{\rho}{\Delta t}) + \theta\hat{\mathcal{L}}^\omega(\rho) = (\omega,\frac{\rho^n}{\Delta t}) - (1-\theta)\hat{\mathcal{L}}^\omega(\rho^n) + \theta(\omega,s) + (1-\theta)(\omega,s^n) + \theta(\omega,h)_{\Gamma_N} + (1-\theta)(\omega,h^n)_{\Gamma_N} \tag{28}$$

In order to avoid instabilities due to the convective part of the equation we introduce the SUPG stabilization (see [15] for more details). We introduce a new term, $s(\omega,\Delta\rho)$, to be added at the left hand side of (25). This new term is defined

$$S(\omega,\rho) = \sum_e \int_{\Omega_e} \mathcal{P}(\omega)\tau\mathcal{R}(\rho)\mathrm{d}\Omega \tag{29}$$

where

$$\mathcal{P}(\omega) = \mathbf{u} \cdot \nabla\omega \quad \text{and} \qquad \mathcal{R}(\rho) = \frac{\rho - \rho^n}{\Delta t} + \theta\mathcal{L}(\rho) + (1-\theta)\mathcal{L}(\rho^n) - [\theta s + (1-\theta)s_n] \tag{30}$$

The choice of the stabilization parameter is a central part of the stabilization scheme. Its definition is not obvious and it is still matter of research. Here we adopt the following expression:

$$\tau = \left(\frac{2}{\Delta t} + \frac{2|\mathbf{u}|}{h} + \frac{4\nu}{h^2} + \sigma\right)^{-1} \tag{31}$$

where h is the mesh size.

3.3 | Spatial Discretization

The spatial discretization of the transport equations are discretized now in space following the Galerkin formulation through out two finite dimensional spaces $\mathcal{S}^h$ and $\mathcal{V}^h$, subsets of $\mathcal{S}$ and $\mathcal{V}$.

$$\mathcal{S}^h = \{\rho \mid \rho(\cdot,t) \in \mathcal{H}^1(\Omega), \rho(\cdot,t)_{|\Omega_e} \in \mathcal{P}_m(\Omega_e)\ t \in [0,T]\ \forall e \text{ and } \rho = \rho^D \text{ on } \Gamma_D\} \text{ and} \tag{32}$$

$$\mathcal{V}^h = \{\omega \in \mathcal{H}^1(\Omega)\ , \omega_{|\Omega_e} \in \mathcal{P}_m(\Omega_e)\ \forall e \text{ and } \omega = 0 \text{ on } \Gamma_D\} \tag{33}$$

where $\mathcal{P}_m$ is the finite element interpolating space. Now the semi-discrete Galerkin formulation is adopted by restricting the weak form to find $\rho^h \in \mathcal{S}^h$ for any $t \in [0,T]$ such that all $\omega^h \in \mathcal{V}^h$ the following fulfills:

$$\begin{aligned}&(\omega^h, \frac{\rho^h}{\Delta t}) + \theta\hat{\mathcal{L}}^h(\rho^h) - (\omega^h, \theta s) - (\omega^h, \theta h) + S^h(\omega^h, \rho^h)\\ &= (\omega^h, \frac{\rho^n}{\Delta t}) - (1-\theta)\hat{\mathcal{L}}^h(\rho^n) + (\omega^h, (1-\theta)s_n) + (\omega^h, (1-\theta)h_n)_{\Gamma_N} + S^n(\omega^h, \rho^n)\end{aligned} \tag{34}$$

where, $S^h(\omega^h, \rho^h)$ and $S^n(\omega^h, \rho^n)$ are such that $S^h(\omega^h, \rho^h) + S^n(\omega^h, \rho^n) = S(\omega^h, \rho^h)$.
By an abuse of notation we have transformed $\hat{\mathcal{L}}^w(\bullet)$ into $\hat{\mathcal{L}}^h(\bullet^h)$ by just replacing our unknowns in the weak form for the ρ^h and ω^h. To clearly define every term, let us expand the term associated with the SUPG stabilization as:

$$\begin{aligned}S^h(\omega^h, \rho^h) &= \mathcal{P}(w)\tau\left[\left(\omega^h, \frac{\rho^h}{\Delta t}\right) + \theta\mathcal{L}^h(\rho^h) - (\omega^h, \theta s_h)\right]\\ S^n(\omega^h, \rho^n) &= \mathcal{P}(w)\tau\left[\left(\omega^h, \frac{\rho^n}{\Delta t}\right) + (1-\theta)\mathcal{L}^h(\rho^n) - (\omega^h, (1-\theta)s_n)\right]\end{aligned} \tag{35}$$

It is worth to note the difference between $\hat{\mathcal{L}}^h(\bullet^h)$ and $\mathcal{L}^h(\bullet^h)$. The latter is an operator in strong form and has a second order differential operator appears, which of course impose important consequences in the following finite element discretization.
The domain Ω is discretized into n_{el} elements named Ω_e. The geometry is interpolated by the shape functions N^i using the nodal positions $\mathbf{x}_i$ with $i = 1..n_{en}$ as

$$\mathbf{x}^h|_{\Omega^e} = \sum_{I=1}^{n_{en}} N^i\, \mathbf{x}_i \tag{36}$$

In the spatial discretization of Ω, a C^0-continuous finite element is used for the density variable ρ. The unknowns quantities ρ are interpolated on the element level in an isoparametric fashion with the shape functions N^i. The test functions ω are also interpolated using the same shape functions as

$$\delta\rho^h|_{\Omega^e} = \sum_{i=1}^{n_{en}} N^i\omega_i \in\ H_1^0(\Omega) \quad \text{and} \quad \rho^h|_{\Omega^e} = \sum_{k=1}^{n_{en}} N^k\rho^k \in\ H_1(\Omega) \tag{37}$$

Following the same interpolation, the gradients of the unknowns and the test functions are written as

$$\nabla\delta\rho^h|_{\Omega^e} = \sum_{i=1}^{n_{en}} \omega_i\nabla N^i \quad \text{and} \quad \nabla\rho^h|_{\Omega^e} = \sum_{k=1}^{n_{en}} \rho^k\nabla N^k \tag{38}$$

and the second order gradient approximations as

$$\nabla^2\delta\rho^h|_{\Omega^e} = \sum_{i=1}^{n_{en}} \omega_i\nabla^2 N^i \quad \text{and} \quad \nabla^2\rho^h|_{\Omega^e} = \sum_{k=1}^{n_{en}} \rho^k\nabla^2 N^k \tag{39}$$

Finally, we will call $\mathbb{B}$ the full set of n_{np} global node points in the finite element discretization described as $\mathbb{B} = \bigcup_{e=1}^{n_{el}} \mathbb{B}^e$ with $\mathbb{B} = \{I \,|\, I = 1, n_{np}\}$. $\mathbb{B}^e$ gathers the complete set of all element nodes n_{el}, $\mathbb{B}^e = \{i \,|\, i = 1, n_{en}\}$. Considering $\mathbb{B}_D$ the set of nodes on the Dirichlet boundary, the approximation ρ^h can be expressed as,

$$\rho^h(\mathbf{x}, t) = \sum_{I \in \mathbb{B}_D} N^I(\mathbf{x}) \rho^D(\mathbf{x}_I) + \sum_{I \in \mathbb{B} \setminus \mathbb{B}_D} N^I(\mathbf{x}) \rho^I \tag{40}$$

Applying the above finite element discretization in space and time we can write the transport equation in the spatial and temporal semi-discretized system of partial differential equations as

$$\left[\frac{\mathbf{M} + \mathring{\mathbf{M}}}{\Delta t}\right] \rho + \theta(\mathcal{L} + \mathring{\mathcal{L}})\rho - [\mathbf{m} + \mathring{\mathbf{m}}][\theta s] = \left[\frac{\mathbf{M} + \mathring{\mathbf{M}}}{\Delta t}\right] \rho^n - (1-\theta)[\mathcal{L} + \mathring{\mathcal{L}}]\rho^n + [\mathbf{m} + \mathring{\mathbf{m}}][(1-\theta)s^n] \tag{41}$$

where

$$\mathcal{L} = \mathbf{m_c} + \mathbf{K} + \sigma \mathbf{M} \text{ and } \mathring{\mathcal{L}} = \mathring{\mathbf{m}}_\mathbf{c} + \mathring{\mathbf{K}} + \sigma \mathring{\mathbf{M}} \tag{42}$$

Each one of the terms in the previous equations can be expanded as

$$\begin{aligned}
\mathbf{M} &= \mathop{\mathbf{A}}_{e=1}^{n_{el}} \int_{\Omega_0^e} N_i N_j \mathrm{d}\Omega, \quad \mathbf{m} = \mathop{\mathbf{A}}_{e=1}^{n_{el}} \int_{\Omega_0^e} N_i \mathrm{d}\Omega, \quad \mathring{\mathbf{m}}_\mathbf{c} = \mathop{\mathbf{A}}_{e=1}^{n_{el}} \int_{\Omega_0^e} \tau \left(\mathbf{u} \cdot \nabla N_i\right) \mathbf{u} \cdot \nabla N_j \mathrm{d}\Omega \\
\mathbf{K} &= \mathop{\mathbf{A}}_{e=1}^{n_{el}} \int_{\Omega_0^e} \nabla N_i \cdot (\nu \nabla N_j) \mathrm{d}\Omega, \quad \mathring{\mathbf{K}} = \mathop{\mathbf{A}}_{e=1}^{n_{el}} \int_{\Omega_0^e} \tau \left(\mathbf{u} \cdot \nabla N_i\right) \cdot (\nu \nabla^2 N_j) \mathrm{d}\Omega, \\
\mathbf{m_c} &= \mathop{\mathbf{A}}_{e=1}^{n_{el}} \int_{\Omega_0^e} N_i \mathbf{u} \cdot \nabla N_j \mathrm{d}\Omega, \; \mathring{\mathbf{M}} = \mathop{\mathbf{A}}_{e=1}^{n_{el}} \int_{\Omega_0^e} \tau \left(\mathbf{u} \cdot \nabla N_i\right) N_j \mathrm{d}\Omega \text{ and } \mathring{\mathbf{m}} = \mathop{\mathbf{A}}_{e=1}^{n_{el}} \int_{\Omega_0^e} \tau \left(\mathbf{u} \cdot \nabla N_i\right) \mathrm{d}\Omega.
\end{aligned} \tag{43}$$

$\mathop{\mathbf{A}}_{e=1}^{n_{el}} \int_{\Omega_0^e}$ denotes the assembly operator acting on the local element matrix and nodal vectors.

4 | COUPLING PROBLEM

In Section 3 we have presented the spatial and temporal discretized form of the general parabolic model. In this section we take the constitutive model of actin treadmilling described in Section 2, apply the numerical approach described in Section 3 and couple them together to end up with a fully coupled system of equations. Once our system of equations has been built we can see that each of the original source terms are now reaction terms with respect to the other equations. Another coupling that appears is through the dependence of convective transport velocity on the magnitude of ρ^a on the leading edge (Eq. (13)). The first coupling is linear in nature, but the second one is non-linear. Hence, the discretized system has to be solved iteratively. A fixed pointed method is used to solve this coupled system. Convergence is not guaranteed for this iterative method and is sensitive to the initial guess, still it is practical option because of its ease implementation. Consider, that we need to find the root of a function $f(x)$, it is first algebraically manipulated to an equivalent form $x = g(x)$. To solve (41), it first needs to be expressed in the equivalent form of $x = g(x)$ as

$$\left[\frac{\mathbf{M} + \mathring{\mathbf{M}}}{\Delta t}\right] \rho^{k+1} + \theta(\mathcal{L}^k + \mathring{\mathcal{L}}^k)\rho^{k+1} - [\mathbf{m} + \mathring{\mathbf{m}}][\theta s^k] = \left[\frac{\mathbf{M} + \mathring{\mathbf{M}}}{\Delta t}\right] \rho^n - (1-\theta)[\mathcal{L}_n + \mathring{\mathcal{L}}_n]\rho^n + [\mathbf{m} + \mathring{\mathbf{m}}][(1-\theta)s^n] \tag{44}$$

The initial guess of ρ is taken as ρ^n. Let ρ^k be the k-th iterate of fixed pointed process. Hence, $\rho^1 = \rho^n$. The iterations continue till the norm of residual of the (44) attains a value below specified tolerance. The last iterate is considered to be the converged solution for the time step $n+1$. After solving (44), ρ^{k+1} is obtained. With this, first the velocities are updated as follows,

$$V_0^{k+1} = k_{on} {\rho^a}^{k+1} (LE, 0) \quad \text{and} \quad V^{k+1} = V_0^{k+1} exp(-F\delta / {\rho^B}^{k+1} k_b T) \tag{45}$$

V^{k+1} is used to update the convection velocity $\mathbf{u}$. The highlighted domain of interest in Fig. 1 is roughly a sector of a circle, as shown in the Fig. 1 . Convection of various constituents happens from leading to trailing edge and the radial edges are assumed to have no fluxes across it. Consequently, in this particular region of the cell, the spatial distribution of the velocity is assumed to be radial and divergence free, as there is no source or sink for the convective fluids, with direction of the velocity in radial direction all over the domain, i.e.

$$\mathbf{u} = V^{k+1} \frac{R}{r} \hat{\mathbf{r}}$$

where the R is the leading edge radius. With the updated velocities (V^{k+1}) and ρ^{k+1}, the operators and sources are evaluated as

$$\mathcal{L}^{k+1} = \mathbf{m_c}(V^{k+1}) + \mathbf{K} + \sigma \mathbf{M} \text{ and } \mathring{\mathcal{L}}^{k+1} = \mathring{\mathbf{m}}_\mathbf{c}(V^{k+1}) + \mathring{\mathbf{K}}(V^{k+1}) + \sigma \mathring{\mathbf{M}}(V^{k+1}) \tag{46}$$

Algorithm 1 Velocity - ρ_a coupling for any given time-step

1: **while** convergence = false **do**
2: Set $V = k_{on}\delta\rho_a(0)\exp(-\delta F/k_B\rho^B T)$ using current iterates of densities ρ_a, ρ^B
3: Set $J_p = \frac{V\rho^B}{\delta\eta}$
4: Apply Neumann B.C: $\nu_a\nabla\rho_a + \mathbf{u}\rho_a = -J_p$
5: Compute new iteration for all densities, ρ_i
6: **end while**

5 | RESULTS

First, we present the results of actin treadmilling in physiological conditions based on the coupling procedure described in previous section, that is considering $J_p = V\rho^B/(\delta\eta)$ and with convective terms. Then we compare the results with the steady-state and non-convective solution described in [29] where the polymerization flux was described as $J_p = Lj_d$. Note that this assumption is only valid for the analytical 1D case and can not be imposed in a general 2D geometry. Then we show the effect of different modified conditions in the dynamics of the retrograde flow. We focus on the effect of the depolymerization, polymerization and nucleation rate, main responsible for the dynamics in the actin turnover and, therefore, in the retrograde flow and cell migration. We further analyze the effect of the membrane resistance, and mechanical variable that has been also described to condition the overall dynamics o the actin flow. We compute numerically a section of the middle part of a keratocyte, as described in Fig. 1 . We analyze the six actin forms described in previous sections. Boundary conditions were also provided which were either zero or a function of the parameters described in Table 1 . The geometry is shown in Fig. 1 (d) and discretized in 20 linear elements in radial and circumferential direction.

5.1 | Actin Treadmilling in Physiological Condition

In this section we consider physiological conditions of motile keratocytes to analyze the patterns of actin within the lamellipodium of the cell. We provide a summary of the parameter values in Table 1 that we consider to represent physiological conditions.

The results at steady-state in the mid section as well as in a line from the front down to the rear of the section are shown in Fig. 2 as it has been recapitulated in theoretical and experimental models [46, 29]. A constant profile of ρ^s and ρ^p is obteined. ρ_a starts at $\approx 10\mu M$ and increases up to $\approx 17\mu M$ and ρ_β starts at $\approx 13.5\mu M$ and increases up to $\approx 15.5\mu M$. The gradient in these two monomers forms induce a diffusion from the back of the cell to the front. Then, we also solve the problem with the assumption of $J_p = Lj_d$ with j_d constant and neglecting the convective terms, as described in [29], instead of the coupling form of the flux we have described above. We plot the differences of the monomeric forms for both descriptions of the flux in Fig. 2 , which are explained in terms of the convection and the change in the polymerization term J_p. We observed a crossing in both variables at $\approx 3.5\mu m$ in our solutions while the spatial distribution of ρ_a and ρ_β in [29] increase uniformly from ≈ 13 and $14\mu M$ up to ≈ 18 and $\approx 20\mu M$, respectively, without the crossing observed in our results. To check if we made any mistake during the FE implementation we also solved the problem with $J_p = Lj_d$ analytically. Our results showed the same behaviour as the FE results. The flux of ATP-actin-profilin at the leading edge is $J_p = 52.26\mu M\mu m s^{-1}$ in comparison with the $J_p = 70\mu M\mu m s^{-1}$ in the analytical solution.

The density of capped minus ends, ρ^{m_c}, is maximum at the leading edge and decreases exponentially up to the trailing edge. Therefore, we describe a capping process occurring mainly in the first 2-4μm from the leading edge after which no more capping occur. This tendency is in agreement with experimental [39] and theoretical results [29]. The density of uncapped minus end, ρ^m, increases from the leading edge and forms a plateau at the rear. The interplay of all the substances provides a protrusion velocity at steady state value of $V = 0.14\mu m s^{-1}$, in agreement with experimental values of fast moving keratocytes [19, 51]

In this physiological conditions we calculate the Peclet number, Pe, as an indicator of the role of advection against diffusion. We found that Pe=0.071, clearly indicates the low role of the advection process in the model. We removed the convective part of the model equations to analyze at what extent the diffusion process dominates the transport of substances in the interior of the cell. The results in Fig. 3 confirm that all concentration remains the same but ρ^β and ρ^a showed minor differences. Although the differences are not remarkable, the increase in the available ATP-G-actin at the leading edge modified the protrusion velocity of the cell to $V = 0.15\mu m s^{-1}$. It presents a barely 7% increase with respect to the inclusion of the advection into the model equations.

Given the low relevance of the convective term in the evolution of the densities in this particular model case, we were also wondering about the effect of the diffusion in the density profiles. Given the different values considered in literature, e.g. D=1.15 $\mu m^2 s^{-1}$ [19] or D=30$\mu m^2 s^{-1}$ [1], we vary the diffusion parameter to D=0.1, 1 and 100 $\mu m^2 s^{-1}$ to analyze the effect of the diffusion parameter as it was done similarly in [19]. As shown in Fig. 4 $\rho^\beta[\mu M]$ and $\rho^a[\mu M]$ increase remarkable in the rear of the lamellipodium as the diffusion coefficient decreases. The decrease in the diffusion coefficient makes the G-actin monomers in the rear of the cell to accumulate since the diffusion of the monomers is diminished by the

low coefficient. ρ^{m_c} increases at the front of the cell, showing an accumulation of capped pointed ends from the leading to the rear edge. Similarly, the uncapped pointed end ρ^m increased close to the leading edge as the diffusivity decreases. Moreover, the protrusion velocity was also modified to $V = 0.03, 0.09, 0.146$ and $0.1437 \mu m s^{-1}$, respectively. These results indicate that as the diffusion coefficient decreases and the monomers start to accumulate in the rear of the cell, the amount of ATP-G-actin in the leading edge decreases and therefore the leading edge velocity decreases. The steady state of the physiological case will be used as the initial conditions for the following simulations.

5.2 | Effect of Depolymerization at the pointed Ends

We simulate the effect of the velocity of depolymerization. Although this is a quantity of difficult measurement experimentally some estimates have been proposed [21, 6] to be in the order of $V_{dep} = 0.1 \mu m s^{-1}$. We explored the effect of varying the depolymerization rate to V_{dep}=0.05 and 0.2 $\mu m s^{-1}$ respectively. Results in Fig. 5 describe the resulting density profiles. When V_{dep}=0.2 increases, we observed an increase of ρ^β and ρ^a across the lamellipodium. As more and more monomers are created at the rear, they diffuse across the lamellipodium increasing the overall amount of monomers in the cell. Similarly, ρ^p and ρ^s increased uniformly. The amount of capped and uncapped minus ends, ρ^m and ρ^{m_c}, also increased. A similar decrease is observed when V_{dep}=0.03 $\mu m s^{-1}$.

5.3 | Effect of the Nucleation rate of Barbed Ends

In sections 5.3 to 5.5 we consider cases of temporal variations of different parameters affecting the treadmilling process, such as those occurring due to externally stimulation using drug treatments. Such stimulations can possibly change one or more model parameters. In each of the following sections we use the steady-state of the physiological conditions described in Section 5.1 as the initial condition, and force a temporal change in one parameter of interest. We assume that an external stimulation would cause the concerned parameter to change in an exponential manner, which slowly settle down, similar to a first order chemical reaction. The temporal change of parameters of interest vary in an exponential manner such that the 99% of the imposed variation is achieved in 30s.

Now, we vary the nucleation rate to describe situation with faster and slower nucleation rates. Slower rates indicate fewer branches in the barbed ends while higher values provide larger number of branches pushing the leading edge. In particular we consider n=100$\mu m^{-1} s^{-1}$ as estimated in [29] and then perform variation to n=50$\mu m^{-1} s^{-1}$ and n=150$\mu m^{-1} s^{-1}$. We first analyze in Fig. 6 how the monomer pool and the actin fibers change due to the variation in the nucleation rate of the barbed ends.

At the front of the cell, we obtained an expected reduction and increase in the density of uncapped leading barbed ends ρ^B when we decrease and increase the nucleation rate respectively. These results were expected on a straight forward revision of the model equations. ρ^β and ρ^a increase a 2.5-fold when the polymerization rate decreased to n=50$\mu m^{-1} s^{-1}$ while decreased at a 60% of its baseline value due to the increase of the polymerization rate to n=150$\mu m^{-1} s^{-1}$. Therefore, the model predicts an increase in the amount of ATP-G-actin in the front when the nucleation rate reduces, since less ATP-G-actin monomers are used at the front for nucleation of the actin filaments. When the nucleation rate increases, the pool of ATP-G-actin also decreases since more monomers are used in the leading edge to promote the F-actin formation. The density variation of these five components were very similar at the back of the cell. However, the variation of the uncapped and capped minus ends was different at the front and rear of the cell. In the rear ρ^{m_c} increase a 2-fold at t=45s when the polymerization rate decreased to n=50$\mu m^{-1} s^{-1}$ while decreased at a 100% of its baseline value due to the increase of the polymerization rate to n=150$\mu m^{-1} s^{-1}$ at t=95s. After, both densities evolved to an stable state of approximately $\rho^{m_c} = 50 \mu m^{-2}$. This behaviour at the rear can be expected as the changes in velocity increases in the whole domain instantaneously, the convection term for ρ^{m_c} appears as a positive source term and ρ^{m_c} first increases. However, at the leading edge the density increases exponentially up to 1550μm^{-2} when the polymerization rate decreases to n=50$\mu m^{-1} s^{-1}$. Similarly, when n=150$\mu m^{-1} s^{-1}$ the density of capped minus ends reduces to 200μm^{-2}.

Then, we investigate the evolution of the densities over time across the thickness of the lamellipodium. In Fig. 7 ρ^a and ρ^β show larger variation when n=50$\mu m^{-1} s^{-1}$ than n=150$\mu m^{-1} s^{-1}$, where the densities variations are negligible. ρ^m and ρ^{m_c} presented larger variation in both cases although increasing or decreasing uniformly from the initial conditions.

Next, we also explore the change in the protrusion velocity along time as the nucleation rate change. Our results in Fig. 8 predict that the protrusion velocity decrease overtime as the nucleation rate increase, and vice versa. When n decreases, ρ^B decreases, and so does the magnitude of flux of ρ^a. As the flux is negative, i.e. going out of the boundary, the outflux decreases, ρ^a increases and consequently the velocity V increases.

5.4 | Effect of Actin Polymerization at the Front of the Cell

Next, we analyze how variations of the rate of monomers assembling affects the turnover process as well as the protrusion velocity (see Fig. 9). Similarly to what we observed for the nucleation rate, we obtained here that as k_{on} is reduced or increased the amount of available ATP-G-actin

increases or decreases. This behavior follows the need for accommodation of larger or lower polymerization rates. Here the densities ρ^B, ρ^s and ρ^p are unaffected. The results on the capped and uncapped pointed ends is however different to previous results. At the leading edge, ρ^{m_c} first increases and then decreases due to the multiple time scales in the problem. Moreover, the density of actin fibers do not include diffusive terms, making the monomer densities to reach steady values faster than the F-actin forms. Both at the leading edge and the rear, ρ^a and ρ^β follows inversely the increase or decrease of k_{on} by a 2- and 1.5-fold, respectively. At the rear, evolution of the F-actin shows the same increase and decrease as reported in the leading edge. However, an inertial-like behavior is observed, where the densities drop or increase below or above the initial values to stabilize, after a short period, at values close to the initial state. The velocity of the leading edge also changed along variation of the polymerization rate. For $k_{on} = 5.8\mu M^{-1}s^{-1}$ we obtained a sudden decrease up to V=0.1μMs^{-1} at t=8s going back to V=0.11μMs^{-1} at the long term. The increase to $k_{on} = 23.2\mu M^{-1}s^{-1}$ increases the protrusion velocity to V=0.13μms^{-1} at t=5s going back to V=0.11μMs^{-1} at the long term.

Then, we investigate the evolution of the densities over time across the thickness of the lamellipodium. Similarly with the previous case, all the densities showed uniform variation across the lamellipodium when the polymerization rate was modified (Fig. 10). ρ^a and ρ^β show larger variation when $k_{on} = 5.8\mu M^{-1}s^{-1}$ than $k_{on} = 23.2\mu M^{-1}s^{-1}$. The variation in ρ^m and ρ^{m_c} were almost negligible and maintain a profile similar to the physiological case. This result could indicate that the increase of ATP-G-actin is redundant and the increase in its content in the leading edge is not used for modifying the barbed ends and the velocity of the cell.

5.5 | Effect of Membrane Resistance

We also explored the effect of the membrane resistance to the actin turnover as well as to the protrusion velocity similarly to previous models [29]. Given the different values reported in literature (see e.g. [43]) we varied up and down the initial value, and the effect is seen in Fig. 11 and 12 . An increase in the membrane resistance would be due to an osmotic shock [9, 30], a sucking micropipette [12] or even obstacle in the cell path. The increase of the membrane resistance to 200pN increased the amount of $\rho^a[\mu M]$ and $\rho^\beta[\mu M]$ at the rear and leading edge of the cell while they decreased as the membrane resistance was decreased up to 50pN. The increase of $\rho^a[\mu M]$ and $\rho^\beta[\mu M]$ would be motivated by the need of higher amount of monomers in the leading edge to keep the protrusion velocity to a physiological value. The associated changes in the protruding velocity would change the flux of ATP-G-actin which would explain the subsequent changes. For F=200pN we obtained an sudden decrease up to V=0.1μMs^{-1} at t=8s going back to V=0.11μMs^{-1} at the long term. The decrease to F=50pN increases the protrusion velocity to V=0.12μms^{-1} at t=5s going back to V=0.11μMs^{-1} at the long term. At the rear the variation showed a similar behavior.

The evolution of the densities over time across the lamellipodium showed a uniform pattern across the lamellipodium when the membrane resistance was modified. Also note that the evolution of the density changes are similar to those observed in Section 5.4 since both parameters appear in the same coupling equation; the expression for the velocity of the cell (see Eq. 20). ρ^a showed a 1.5-fold increase and 0.75-fold decrease when F=200pN and F=50pN, respectively. The decrease and increase of ρ^β was barely a 10% when the membrane resistance was increased or decreased. The variation in ρ^m and ρ^{m_c} where almost negligible and maintain a profile similar to the physiological case. These results indicate that the variation in the membrane resistance affect the pool of actin monomers and not the dynamics of the minus ends. The velocity of the leading edge was kept constant along the different membrane resistances.

Finally, we analyzed the coupled effect of the membrane resistance and the nucleation rate in the protrusion velocity of the cell, similarly to previous founds [29]. Fig. 13 predict a maximum velocity for each membrane resistance. Note that this is equivalent to plot the velocity as a function of ρ^B. For F=200pN the maximum protrusion velocity (V=0.345$\mu m/s$) is achieved for n=30. When increasing to a membrane resistance F=100pN the maximum velocity (V=0.57$\mu m/s$) is achieved for n=16 while for F=50pN and n=10 the maximum velocity of V=0.92$\mu m/s$ is obtained. The maximum velocity and the associated nucleation rates establish a limit for which an increase or decrease of the nucleation rate will lead to a decrease of the protrusion velocity. The constant velocity described previously for the different membrane resistance can be observed here for the value of n=100. In table 2 we show a comparison of our results and those found in [29]. The results do not match exactly although the pattern is very similar. For the different membrane resistances we found that the maximum velocity is higher, and is achieved at lower nucleation rates. The fully coupled approach adopted here, where both time and convective terms are included and where no simplifications in the analysis of the equation were adopted, would explain the quantitative differences in the theoretical and computational approach. The effect of the advection terms as we change the nucleation rate and, therefore, the polymerization flux and the velocity could be the reason of these differences. The variation in the density profiles when the advection is turned on or off in the model is almost negligible at the base case. Note that at $n = 100\mu m^{-1}s^{-1}$ our results for the velocity closely match the analytical results. However, as we move away from that specific case, the effect of the varying velocity in the convective terms modifies the overall response.

6 | DISCUSSION

The retrograde flow is a continuous movement of cellular elements from the outer margin of the cell, the leading edge, to the back of the cell. The retrograde flow has been directly related to cell motility [7, 33]. The leading edge protrusions arising in the cell membrane are also in charge of the cell movement. During this intriguing and well orchestrated coupling of cellular elements, actin treadmilling has been shown as one of the most determining processes for the retrograde flow. And, among them, actin treadmilling and the forces generated by the myosin motors are key to generate the retrograde flow and motion of the cell.

Apart from tremendous achievements in experimental cell biology in terms of understanding the retrograde flow, mathematical and computational models have kept well behind the achievements of its experimental counterparts. Mathematical and computational models (see, e.g. [16, 13] for some reviews) are highly reliable, reproducible and low-cost tools that can help to unravel many of the open questions in cellular biology. For example, the measurement protocols of each individual G-actin forms are not fully developed and the spatial and temporal quantification over the lamellipodium is complicated to measure experimentally. In this regard, e.g, computational models can provide new insights in cell motility.

In this work, we focused mainly in fast motile cells. In slow motile migrating cells, the polymerization rate should be high enough to favor a low protrusion velocity of the leading edge, independently of the membrane resistance. We adopted one of the most advance and accurate models in literature [29]. Our goal was to move forward and analyze the complex behavior of the actin treadmilling through numerical approaches. We aimed to describe the non-uniform spatial and temporal evolution of the actin treadmilling involved in cell motility and solve phenomena that are not possible through analytical solutions. We implemented a classical finite element scheme for parabolic equation to account for the unsteady and convective nature of the model as well as the reaction and source terms. The numerical model described here allowed for a more flexible description of the problem compared with previous contributions [29]. It allowed us to measure the time evolution of all the quantities over time and along space when the physical quantities of the problem, related to the kinetics of the actin treadmilling, were modified.Although for some cells the convective velocity is relatively low compared with the diffusion (low Pe), in other circumstances (higher retrograde flows) and regions (those where flow speeds up due to the effect of myosin or due to geometric features) it may play a more critical role. Therefore, we included the convective term and its stabilization to account for an eventual numerical difficulties. Although the inclusion of the convective term and its numerical stabilization is not required in most of the situations, its inclusion is neither in detrimental of the modeling capabilities of the retrograde flow and, in fact, it provides a more general description of the transport problem. The general numerical scheme, although well set in literature, has never been described for models of actin treadmilling. We have included a version of the code at http://www.lacan.upc.edu.

In the physiological state, our results are comparable to those reported in [29]. We first solved the problem with the assumption of $J_p = Lj_d$, with j_d constant, and neglecting the convective terms as in [29]. Then, we use our FE framework to impose a velocity-dependent polymerization flux, as also indicated by [29] and to be able to analyze situation here the model parameters change from those defined for the physiological case. We reproduce some of the results described in [29], which at the same time are in agreement with experimental observations [39, 19, 51]. We found a strong correlation with the diffusion coefficient of the G-actin transport, indicating its key role of the dynamics of the actin monomers in the migration of the cell. However, we also found that our analytical solution varies from the results reported in [29]. Besides a change at the beginning and ending of the density profiles, we observed a crossing of ρ_α and ρ_β at $\approx 3.5\mu m$. We also solved the assumptions of the simplified model analytically and we found the same behaviour of the densities across the lamellipodium than in our FE solution. Although it was not possible to track down the origin of these discrepancies, the main quantitative and qualitative features of the model are reproduced within the range of values reported in experimental observations.

Then we moved forward to hypothesize eventual responses in space and time due to the easily manipulation of the cellular mechanisms within a computational framework. We use our time dependent FE framework with convective terms as well as the velocity-dependent polymerization, $J_p = V\rho^B/(\delta\eta)$, to investigate the effect of different parameter scenarios. Note that this assumption was also used in [29] to anaylze the optimum velocity as a function of ρ^B, but it was not used to analyze the density profiles for different values other than n=100$\mu m^{-1}s^{-1}$. If the flux $J_p = Lj_d$ is used to analyze the dependency of the velocity to the nucleation rate a monolitic increase is observed. If $J_p = V\rho^B/(\delta\eta)$ is used, as in [29] and in our results, different results are obtained. Therefore, we have been able to impose the velocity-dependent polymerization flux to account for a large range of model parameters. We have shown that changing the assumptions made for the convective and specially for the polymerization flux we obtain quantitive different actin densities in the lamellipodium of the cell. However, the results obtained for both approaches are still within the range of experimental observation and, therefore, further theoretical and experimental work will be required in the future. Then, we provided numerical results of transient effects of different biological quantities of our system; the protrusion velocity and actin density profiles.

We described how variations of the actin treadmilling rates change the velocity of the leading edge and the density of actin monomers and filaments along time. We observed complex trends in the G-actin and F-actin dynamics, both spatially and temporally. Given the time-dependent parameters involved in the model and the time variations of the rates of interest, we obtained a dynamic response of the associated actin forms. Actin monomer variations in time both at the rear and the leading edge followed the exponential variations of the treadmilling rate variables, in the range of $\approx 30sec.$ The F-actin forms, however, vary rapidly along time, in the range of $\approx 10sec.$, indicating a differential time response of actin G- and F-actin due to the variations in the internal rates of polymerization or depolymerization. We also analyzed the effect of the convective term in the dynamics of actin treadmilling. Although, as we described before, the convective terms is mostly negligible with respect to the diffusion of the monomers, we believe that the effect of the velocity in the coupling with the flux of ATP-G-actin-profilin in the boundary may be more relevant for the dynamics of the actin treadmilling out of the physiological case. In fact, the discrepancies we found in the velocity with respect to the variation of the nucleation rate are due to the inclusion of the convective terms. In any case, and apart from small quantitative differences, the computational approach reassemble the qualitative finding in [29]. All these aspects focus on the relevance and, at the same time, the complexity of mathematical models of actin treadmilling and the need of further experimental validation. We hope to have provided a new flexible and easily extendible finite element framework for the physical modeling and analysis of the actin treadmilling problem.

The current model is the first of further developments of finite element modeling on actin dynamics. First of all, the model is easily extendable to other mechanisms of actin treadmilling. Further interactions, such as active forces or adhesion mechanisms, can be introduced in a straightforward fashion. When coupled with mechanical equations, models would be able to account for the movement, crawling and polarization of the cell. We believe that the inclusion of the mechanics of the fluid as well as the substrate adhesion could provide new insights in the fascinating phenomenon of cell migration. A fully coupled model of all these ingredients is still missing in literature and should be the focus of our attention in future developments.

7 | ACKNOWLEDGMENTS

K.S and P.M have been financially supported by the Erasmus Mundus programme of the European Commission under the Convection Number 2013-0220. P.S. has been financially supported by the Spanish Ministry of Economy and Competitiveness (MiNeCo) under grants K-00555 and DPI2016-74929-R, and by Generalitat de Catalunya under grants 2014-SGR-1471 and 2017-SGR-1278.

References

[1] Abraham, V.C., Krishnamurthi, V., Taylor, D.L. and Lanni, F. The actin-based nanomachine at the leading edge of migrating cells. Biophys. J., 77(3):1721–1732, 1999.

[2] Amann, K.J. and Pollard, T.D. The Arp2/3 complex nucleates actin filament branches from the sides of pre-existing filaments. Nat. Cell Biol., 3(3):306–310, 2001.

[3] Barnhart, E.L., Lee, K.C., Keren, K., Mogilner, A. and Theriot, J.A. An adhesion-dependent switch between mechanisms that determine motile cell shape. PLoS Biol., 9(5), 2011.

[4] Bindschadler, M., Osborn, E.A., Dewey, C.F. and McGrath, J.L. A mechanistic model of the actin cycle. Biophys J, 86(5):2720–2739, 2004.

[5] Campellone, K.G. and Welch, M.D. A nucleator arms race: cellular control of actin assembly. Nat. Rev. Mol. Cell Biol., 11(4):237–51, 2010.

[6] Carlier, M.F., Laurent, V., Santolini, J., Melki, R., Didry, D., Xia, G.X., Hong, Y., Chua, N.H. and Pantaloni, D. Actin Depolymerizing Factor (ADF/Cofilin) Enhances the Rate of Filament Turnover: Implication in Actin-based Motility. J. Cell Biol., 136(6):1307–1322, 1997.

[7] Cramer, L.P. Molecular mechanism of actin-dependent retrograde flow in lamellipodia of motile cells. Front. Biosci., 2(Fig 2):d260–d270, 1997.

[8] Edwards, M., Zwolak, A., Schafer, D.A., Sept, D., Dominguez, R. and Cooper, J.A. Capping protein regulators fine-tune actin assembly dynamics. Nat. Rev. Mol. Cell Biol., 15(10):677–89, 2014.

[9] Gauthier, N.C., Fardin, M.A., Roca-Cusachsa, P., Sheetz, M.P. Temporary increase in plasma membrane tension coordinates the activation of exocytosis and contraction during cell spreading. Proc. Natl. Acad. Sci. U. S. A., 108(35):14467–14472,2011.

[10] Ghosh, M., Song, X., Mouneimne, G., Sidani, M., Lawrence, D.S. and Condeelis, J.S. Cofilin promotes actin polymerization and defines the direction of cell motility. Science, 304(5671):743–746, 2004.

[11] Grimm, H.P., Verkhovsky, A.B., Mogilner, A. and Meister, J.J. Analysis of actin dynamics at the leading edge of crawling cells: Implications for the shape of keratocyte lamellipodia. Eur. Biophys. J., 32(6):563–577, 2003.

[12] Hochmuth, R.M. Micropipette aspiration of living cells. J. Biomech. 33:15–22,2000.

[13] Holmes, W.R. and Edelstein-Keshet, L. A Comparison of Computational Models for Eukaryotic Cell Shape and Motility. PLoS Comput. Biol., 8(12), 2012.

[14] Honda, H., Nagashima, H. and Asakura, S. Directional movement of F-actin in vitro. J. Mol. Biol., 191(1):131–133, 1986.

[15] Donea, J. and Huerta, A. Finite Element Methods for Flow Problems. Wiley, 2003.

[16] Jilkine, A. and Edelstein-Keshet, L. A comparison of mathematical models for polarization of single eukaryotic cells in response to guided cues, 2011.

[17] Jurado, C., Haserick, J.R. and Lee, J. Slipping or Gripping? Fluorescent Speckle Microscopy in Fish Keratocytes Reveals Two Different Mechanisms for Generating a Retrograde Flow of Actin. Mol. Biol. Cell, 16(2):507–518, 2004.

[18] Liu, W.K., Liu, Y., Farrell, D., Zhang, L., Wang, X.S., Fukui, Y., Patankar, N., Zhang, Y., Bajaj, C., Lee, J. and Hong, J. Immersed finite element method and its applications to biological systems. Comput Method Appl M, 195:1722–1749, 2006.

[19] Keren, K., Yam, P.T., Kinkhabwala, A., Mogilner, A. and Theriot, J.A. Intracellular fluid flow in rapidly moving cells. Nat. Cell Biol., 11, 2009.

[20] Lai, F.P., Szczodrak, M., Block, J., Faix, J., Breitsprecher, D., Mannherz, H.G., Stradal, T.E., Dunn, G.A., Small, J.V. and Rottner, K. Arp2/3 complex interactions and actin network turnover in lamellipodia. EMBO J., 27(7):982–92, 2008.

[21] Lappalainen, P. and Drubin, D.G. Cofilin promotes rapid actin filament turnover in vivo Cofilin promotes rapid actin filament turnover in vivo. Nature, 389(September):1–6, 1997.

[22] Lew, D.J. Formin' actin filament bundles. Nat. Cell Biol., 4(2):E29–30, 2002.

[23] Lewalle, A., Fritzsche, M., Wilson, K., Thorogate, R., Duke, T. and Charras, G. A phenomenological density-scaling approach to lamellipodial actin dynamics. Interface Focus, 4:20140006, 2014.

[24] Lin, C.H., Espreafico, E.M., Mooseker, M.S. and Forscher, P. Myosin Drives Retrograde F-Actin Flow in Neuronal Growth Cones. Neuron, 16(4):769–782, 1996.

[25] Lin, C.H. and Forscher, P. Growth cone advance is inversely proportional to retrograde F-actin flow. Neuron, 14(4):763–771, 1995.

[26] Lomakin, A.J., Lee, K.C., Han, S.J., Bui, D.A., Davidson, M., Mogilner, A. and Danuser, G. Competition for actin between two distinct F-actin networks defines a bistable switch for cell polarization. Nat. Cell Biol., 17(August):DOI: 10.1038/ncb3246, 2015.

[27] Mitchison, T.J. and Cramer, L.P. Actin-based cell motility and cell locomotion, 1996.

[28] Mogilner, A. and Oster, G. Cell motility driven by actin polymerization. Biophys. J., 71(6):3030–45, 1996.

[29] Mogilner, A. and Edelstein-Keshet, L. Regulation of actin dynamics in rapidly moving cells: a quantitative analysis. Biophys. J., 83(3):1237–1258, 2002.

[30] Mueller, J. et al. Load Adaptation of Lamellipodial Actin Networks. Cell., 171:1–13, 2017.

[31] Mullins, R.D., Heuser, J.A. and Pollard, T.D. The interaction of Arp2/3 complex with actin: nucleation, high affinity pointed end capping, and formation of branching networks of filaments. Proc. Natl. Acad. Sci. U. S. A., 95(11):6181–6186, 1998.

[32] Pantaloni, D., Boujemaa, R., Didry, D., Gounon, P. and Carlier, M.F. The Arp2/3 complex branches filament barbed ends: functional antagonism with capping proteins. Nat. Cell Biol., 2(7):385–391, 2000.

[33] Pantaloni, D., Le Clainche, C. and Carlier, M.F. Mechanism of actin-based motility. Science (80-.)., 292(May):1502–1506, 2001.

[34] Peskin, C.S., Odell, G.M. and Oster, G.F. Cellular motions and thermal fluctuations: the Brownian ratchet. Biophys. J., 65(1):316–24, 1993.

[35] Pollard, T.D. Rate constants for the reactions of ATP-and ADP-actin with the ends of actin filaments. J. Cell Biol., 103(6):2747, 1986.

[36] Pollard, T.D., Blanchoin, L. and Mullins, R.D. Molecular mechanisms controlling actin filament dynamics in nonmuscle cells. Annu. Rev. Biophys. Biomol. Struct., 29:545–576, 2000.

[37] Pollard, T.D. and Borisy, G.G. Cellular motility driven by assembly and disassembly of actin filaments, 2003.

[38] Pollard, T.D. and Cooper, J.A. Actin, a central player in cell shape and movement. Science, 326(5957):1208–12, 2009.

[39] Ponti, A., Machacek, M., Gupton, S.L., Waterman-Storer, C.M. and Danuser, G. Two Distinct Actin Networks Drive the Protrusion of Migrating Cells. Science (80-.)., 305(5691):1782–1786, 2004.

[40] Rüberg, T. and Aznar, J.M.G. Numerical simulation of solid deformation driven by creeping flow using an immersed finite element method, volume 0123456789. Springer International Publishing, 2016.

[41] Schaus, T.E., Taylor, E.W. and Borisy, G.G. Self-organization of actin filament orientation in the dendritic-nucleation / array-treadmilling model. PNAS, 104(17), 2007.

[42] Shao, D., Levine, H. and Rappel, W.J. Coupling actin flow, adhesion, and morphology in a computational cell motility model. Proc. Natl. Acad. Sci., 109(18):6851–6856, 2012.

[43] Sheetz, M. P., Dai, J. Modulation of membrane dynamics and cell motility by membrane tension. Trends Cell Biol., 6(3):85-89, 1996.

[44] Shi, Y., Kirwan, P., Smith, J., Robinson, H.P. and Livesey, F.J. Human cerebral cortex development from pluripotent stem cells to functional excitatory synapses. Nat. Neurosci., 15(3):477–86, S1, 2012.

[45] Svitkina, T.M., Verkhovsky, A.B., McQuade, K.M. and Borisy, G.G. Analysis of the actin-myosin II system in fish epidermal keratocytes: Mechanism of cell body translocation. J. Cell Biol., 139(2):397–415, 1997.

[46] Theriot, J.A. and Mitchison, T.J. The rate of actin-based motility of intracellular Listeria monocytogenes equals the rate of actin polymerization. Nature, 357(6375):257–260, 1992.

[47] Theriot, J.A. and Mitchison, T.J. Actin microfilament dynamics in locomoting cells., 1991.

[48] Vallotton, P., Danuser, G., Bohnet, S., Meister, J.J. and Verkhovsky, A.B. Tracking retrograde flow in keratocytes: news from the front. Mol. Biol. Cell, 16(3):1223–1231, 2005.

[49] Wang, Y.L. Exchange of actin subunits at the leading edge of living fibroblasts: Possible role of treadmilling. J. Cell Biol., 101(2):597–602, 1985.

[50] Welch, M.D., DePace, A.H., Verma, S., Iwamatsu, A. and Mitchison, T.J. The human Arp2/3 complex is composed of evolutionarily conserved subunits and is localized to cellular regions of dynamic actin filament assembly. J. Cell Biol., 138(2):375–384, 1997.

[51] Wilson, C.A., Tsuchida, M.A., Allen, G.M., Barnhart, E.L., Applegate, K.T., Yam, P.T., Ji, L., Keren, K., Danuser, G. and Theriot, J.A. Myosin II contributes to cell-scale actin network treadmilling through network disassembly. Nature, 465(7296):373–7, 2010.

[52] Yam, P.T., Wilson, C.A., Ji, L., Hebert, B., Barnhart, E.L., Dye, N.A., Wiseman, P.W., Danuser, G. and Theriot, J.A. Actin-myosin network reorganization breaks symmetry at the cell rear to spontaneously initiate polarized cell motility. J. Cell Biol., 178(7):1207–1221, 2007.

Parameter [Units]		Ref.	Parameter [Units]		Ref.
δ [nm]	2.2	[29]	$\eta[\mu M^{-1}\mu m^{-2}]$	100	[29]
n $[\mu m^{-1}s^{-1}]$	100	[29]	k_{on} $[\mu M^{-1}s^{-1}]$	11.6	[35]
k_BT [pN nm]	4.1	[34]	F [pN/μm]	100	[43]
j_d μMs^{-1}	7	[29]	D $\mu m^2 s^{-1}$	30	[29]
γ $[s^{-1}]$	1	[36]	$k_1[s^{-1}]$	2	[29]
k_{-1} $[s^{-1}]$	10	[29]	$k_2[s^{-1}]$	20	[29]
$k_3[s^{-1}]$	2	[29]	km_3 $[s^{-1}]$	2	[29]
t_1 [s]	30	[29]	t_2 [s]	1	[29]

TABLE 1 Parameters values of the treadmilling models which are considered for physiological condition of the migrating cell.

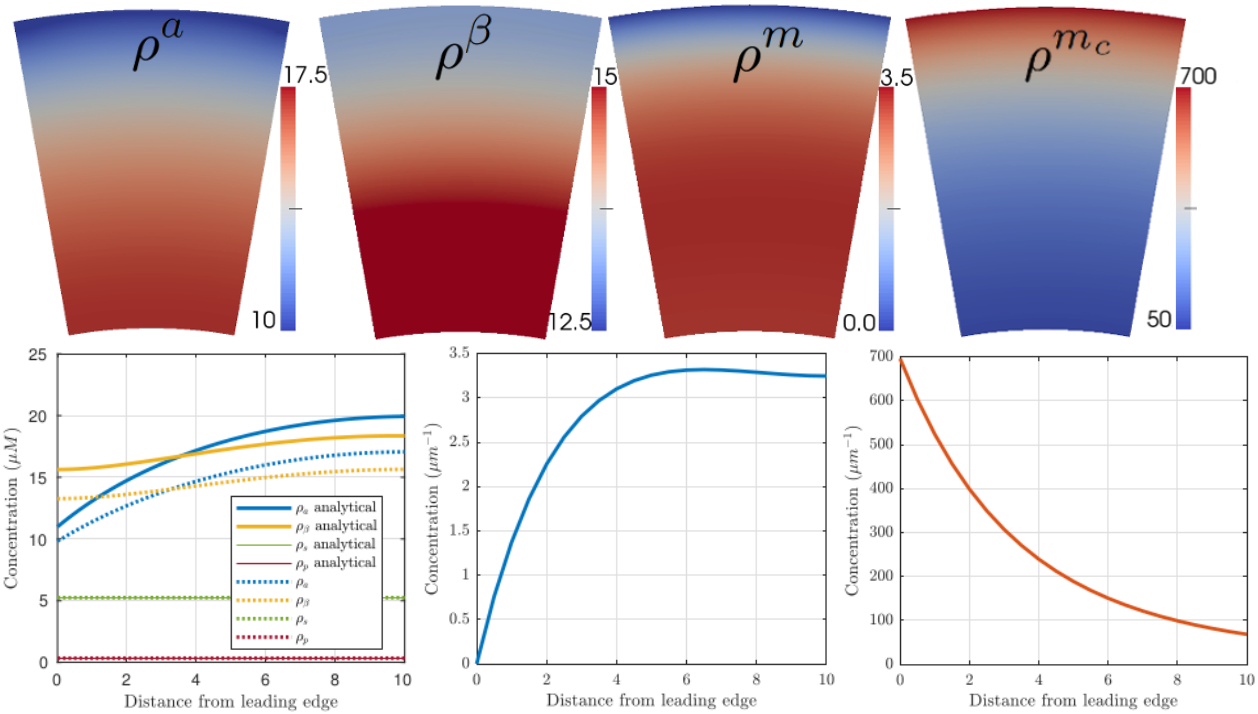

FIGURE 2 Concentration of G-actin and F-actin at the considered physiological conditions. Concentration of actin monomers $\rho^\beta[\mu M]$ and $\rho^a[\mu M]$, $\rho^s[\mu M]$, $\rho^p[\mu M]$ and filaments $\rho^m[\mu m^{-2}]$ and $\rho^{m_c}[\mu m^{-2}]$ in the domain of analysis (top). Evolution of the densities of monomers (bottom, left), and filaments $\rho^m[\mu m^{-2}]$ (bottom, center) and $\rho^{m_c}[\mu m^{-2}]$ (bottom, right) along a line from the front to the rear of the cell, distance in μm.

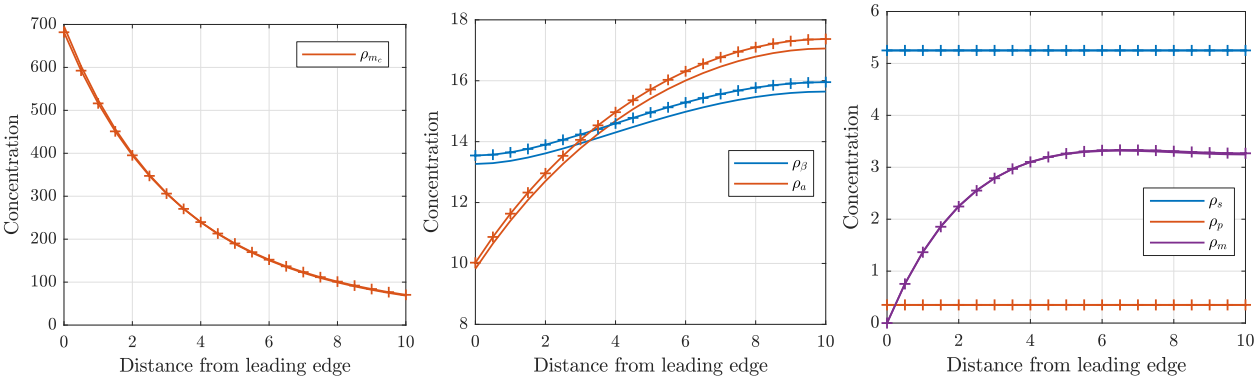

FIGURE 3 Concentration of G-actin and F-actin when the convective term of the model equation is neglected (+) when it is not (-). Concentration of actin monomers $\rho^\beta[\mu M]$ and $\rho^a[\mu M]$, $\rho^s[\mu M]$, $\rho^p[\mu M]$ and filaments $\rho^m[\mu m^{-2}]$ and $\rho^{m_c}[\mu m^{-2}]$ along a line from the front to the rear of the cell, distance in μm.

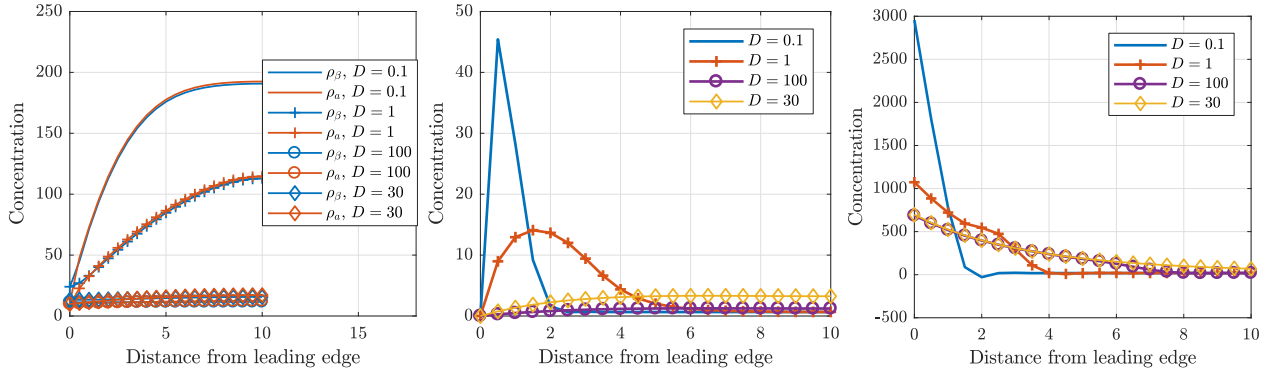

FIGURE 4 Concentration of actin monomers $\rho^\beta[\mu M]$ and $\rho^a[\mu M]$ and filaments $\rho^m[\mu m^{-2}]$ and $\rho^{m_c}[\mu m^{-2}]$ along a line from the front to the rear of the cell when the diffusion coefficient varies, distance in μm.

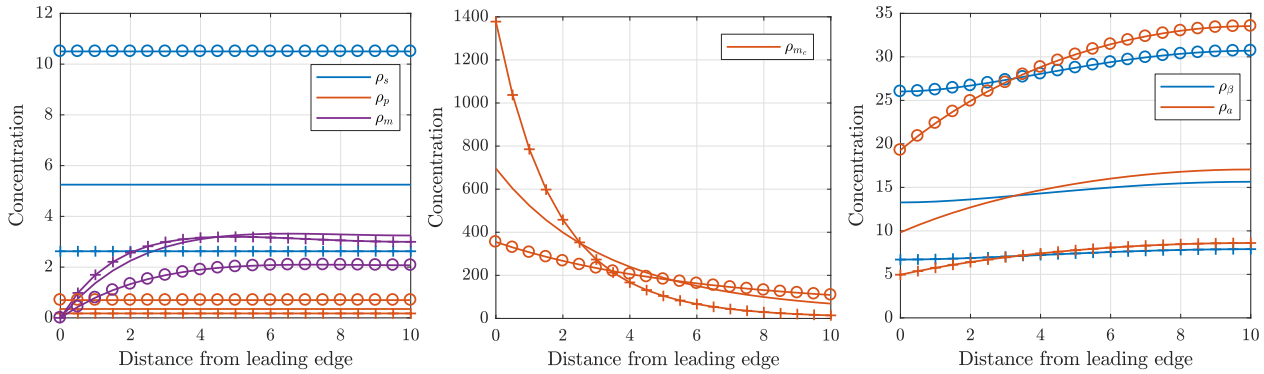

FIGURE 5 Concentration of G-actin and F-actin at different condition of the depolymerization velocity, V_{dep}=0.05, 0.1 and 0.2 $\mu m s^{-1}$ represented with crosses(+), lines(−) and circles(*o*) respectively. Concentration of actin monomers $\rho^\beta[\mu M]$ and $\rho^a[\mu M]$, $\rho^s[\mu M]$, $\rho^p[\mu M]$ and filaments $\rho^m[\mu m^{-2}]$ and $\rho^{m_c}[\mu m^{-2}]$ along a line from the front to the rear of the cell (bottom), distance in μm.

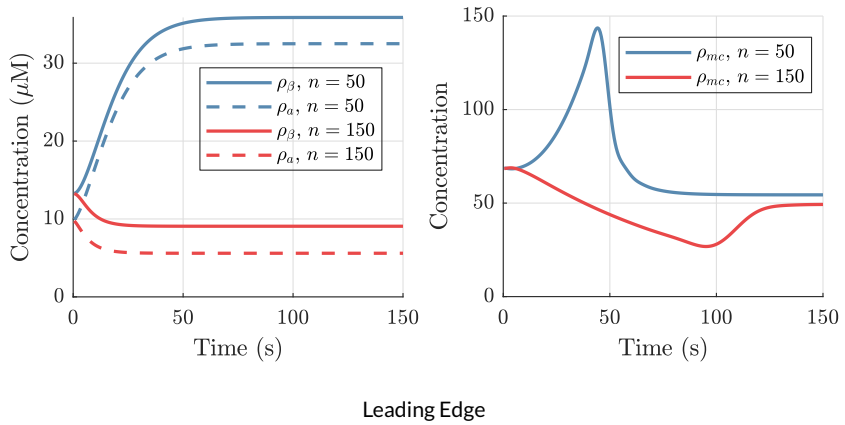

FIGURE 6 Time evolution of filaments at front (top) and rear (bottom) ρ^m, ρ^a and ρ^β, ρ^{mc} and ρ^B across the lamellipodium at different times when $n = 50 \mu m^{-1} s^{-1}$ (black) and $n = 150 \mu m^{-1} s^{-1}$ (black).

Membrane resistance	Velocity [29] (Velocity [our findings])	Nucleation rate [29] (Nucleation rate [our findings])
F = 200 [pN]	0.18 (0.35) [$\mu m s^{-1}$]	59 (30) [$\mu m^{-1} s^{-1}$]
F = 100 [pN]	0.27 (0.57) [$\mu m s^{-1}$]	36 (16) [$\mu m^{-1} s^{-1}$]
F = 50 [pN]	0.39 (0.92) [$\mu m s^{-1}$]	22 (10) [$\mu m^{-1} s^{-1}$]

TABLE 2 Comparison of optimal values of leading edge velocity and nucleation rate with [29]

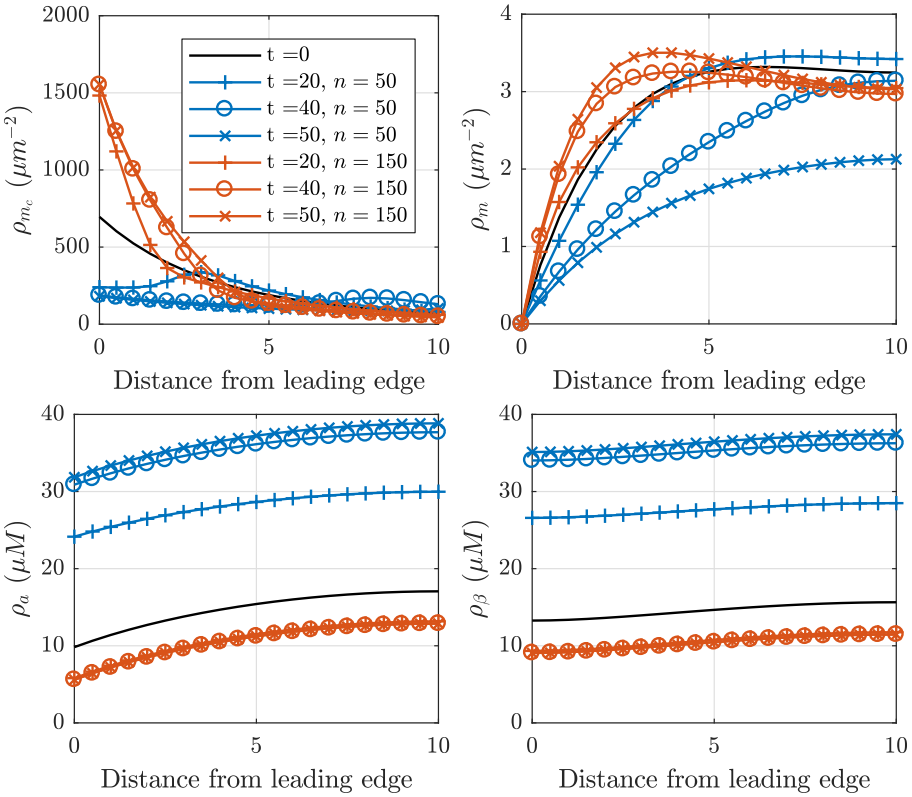

FIGURE 7 Concentration of filaments $\rho^m[\mu m^{-2}]$ and $\rho^{m_c}[\mu m^{-2}]$ and actin monomers $\rho^a[\mu M]$ and $\rho^\beta[\mu M]$ along a line from the front to the rear of the cell when the nucleation rate is varied from physiological conditions ($n = 100\mu m^{-1}s^{-1}$) to $n = 50\mu m^{-1}s^{-1}$ (black) and $n = 150\mu m^{-1}s^{-1}$ (brown), distance in μm.

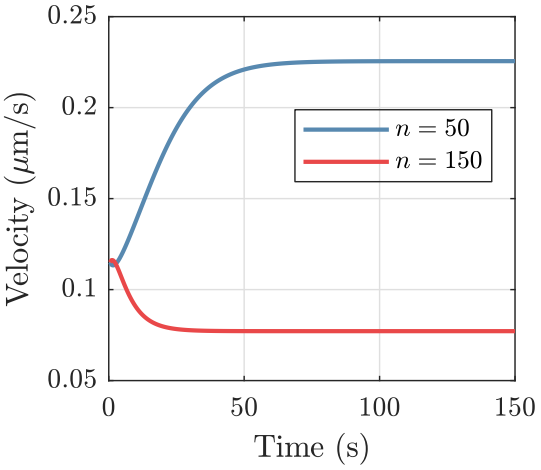

FIGURE 8 Varation of the protrusion velocity from the physiological case, due to an increase and decrease to $n = 150\mu m^{-1}\, s^{-1}$ (black) and $n = 50\mu m^{-1}s^{-1}$ (black) respectively. For $n = 50\mu m^{-1}s^{-1}$ we obtained an increase to $V = 0.225\mu m\, s^{-1}$ while the increase to $n = 150\mu m^{-1}s^{-1}$ reduce the protrusion velocity to $V = 0.077\mu m\, s^{-1}$.

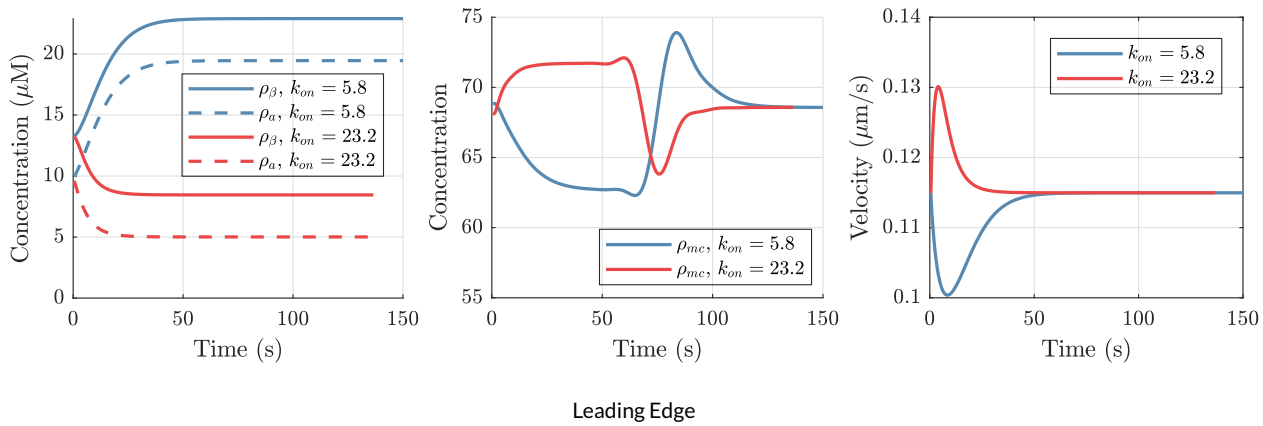

FIGURE 9 Concentration of actin monomers at the leading (top) and rear edge (bottom) $\rho^{\beta}[\mu M]$ and $\rho^{a}[\mu M]$ and filaments $\rho^{m}[\mu m^{-2}]$ and $\rho^{m_c}[\mu m^{-2}]$ when the actin polymerization rate changes, distance in μm. In the top right figure, variation of the protrusion velocity from the baseline case. Lines show variation with respect to the baseline case, $k_{on} = 11.6\mu M^{-1}s^{-1}$ [35], due to an increase and decrease to $k_{on} = 5.8\mu M^{-1}s^{-1}$ (black) and $k_{on} = 23.2\mu M^{-1}s^{-1}$ (black) respectively. The actin polymerization rate is changed from the physiological value to the said values, exponentially in time interval of $30s$

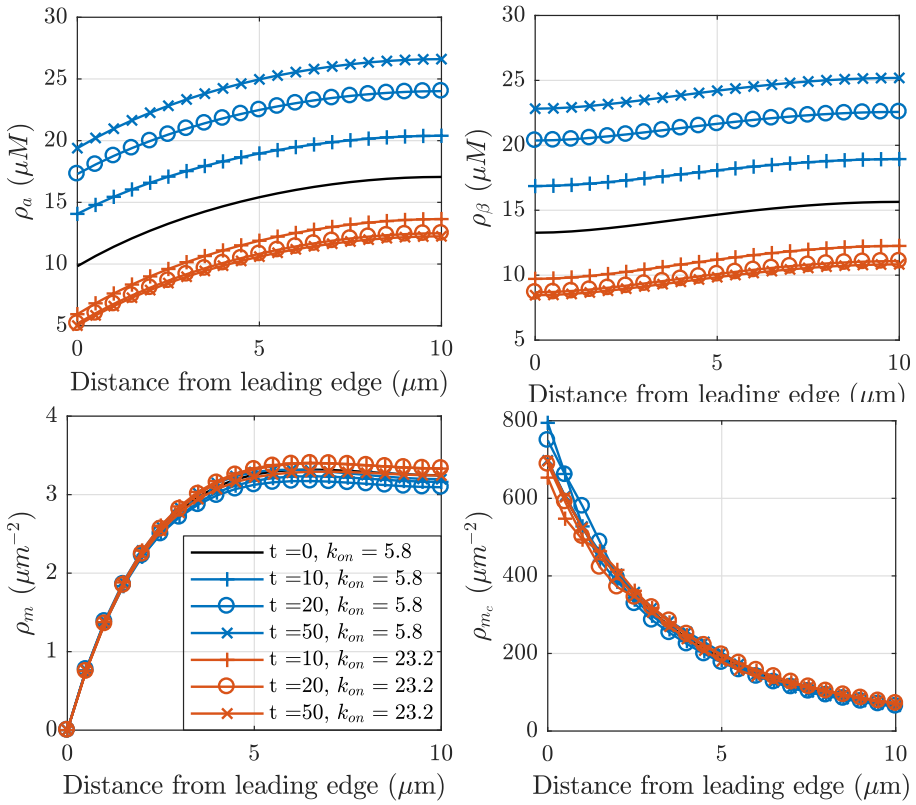

FIGURE 10 Time evolution snapshots of $\rho^{a}[\mu M]$, $\rho^{\beta}[\mu M]$ and filaments $\rho^{m}[\mu m^{-2}]$ and $\rho^{m_c}[\mu m^{-2}]$ across the lamellipodium at different times, with changes in protrusion velocity from physiological value to $k_{on} = 5.8\mu M^{-1}s^{-1}$ (black) and $k_{on} = 23.2\mu M^{-1}s^{-1}$ (brown), exponentially in $30s$.

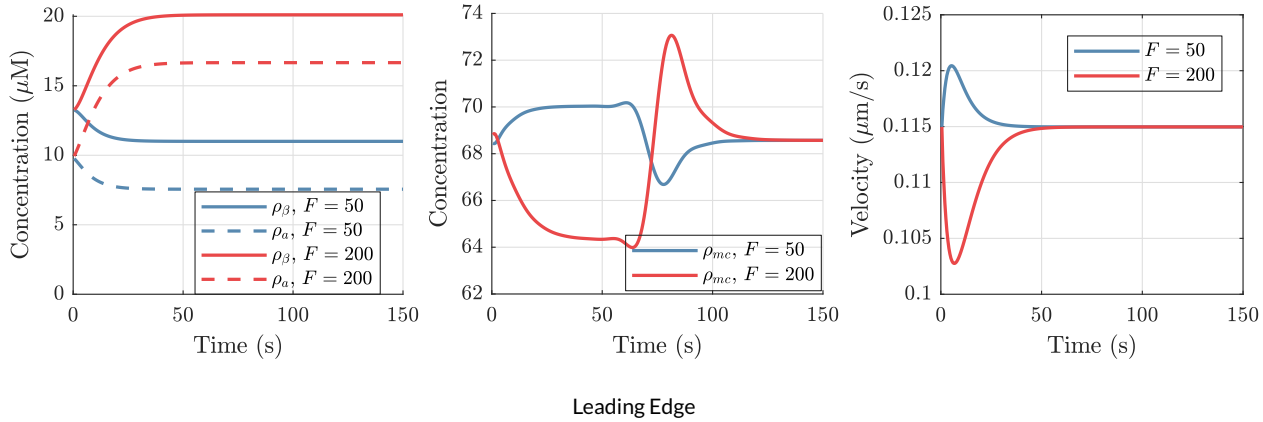

FIGURE 11 Concentration of actin monomers at the leading edge (top) and rear edge (bottom) of the cell $\rho^{\beta}[\mu M]$ and $\rho^{a}[\mu M]$ and filaments $\rho^{m}[\mu m^{-2}]$ and $\rho^{m_c}[\mu m^{-2}]$ when the membrane resistance is modified from physiological value of $100pN\mu m^{-1}$ to $50pN\mu m^{-1}$(black) and $200pN\mu m^{-1}$(black). In the top right figure, variation of the protrusion velocity from the baseline case due to an increase and decrease of the membrane resistance.

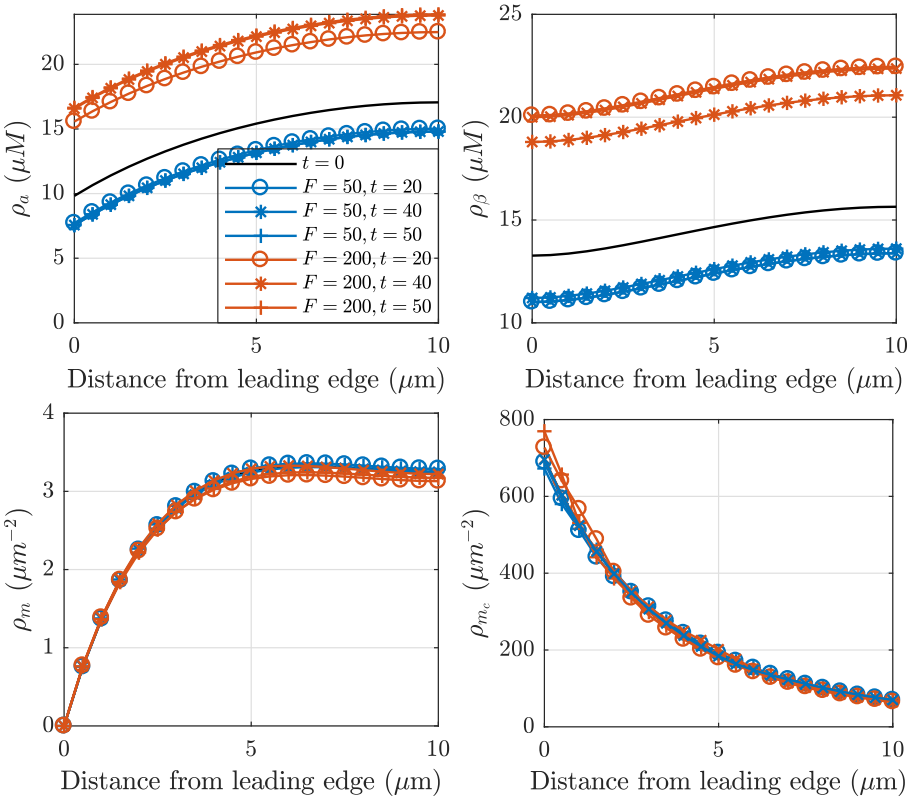

FIGURE 12 Time evolution snapshots of $\rho^{\beta}[\mu M]$ and $\rho^{a}[\mu M]$ and filaments $\rho^{m}[\mu m^{-2}]$ and $\rho^{m_c}[\mu m^{-2}]$ across the lamellipodium, when the membrane resistance is changed from physiological value of $100pN\mu m^{-1}$ to $50pN\mu m^{-1}$(black) and $200pN\mu m^{-1}$(brown), exponentially in $30s$

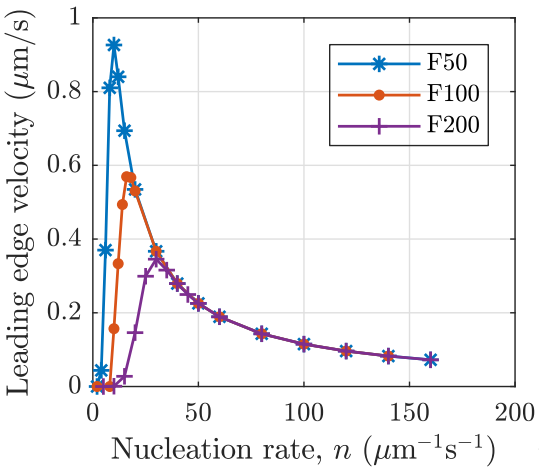

FIGURE 13 Variation of the leading edge velocity as a function of the membrane resistance and the nucleation rate.